Structural, electronic, and energetic properties of SiC[111]/ZrB_2[0001] heterojunctions: A first-principles density functional theory study

Po-Liang Liu,[1] A. V. G. Chizmeshya,[2] and John Kouvetakis[2]

[1]*Institute of Precision Engineering, National Chung Hsing University, Taichung, Taiwan 402, Republic of China and Center for Advanced Industry Technology and Precision Processing, National Chung Hsing University, Taichung, Taiwan 402, Republic of China*

[2]*Department of Chemistry and Biochemistry, Arizona State University, Tempe, Arizona 85287-1604, USA*

(Received 7 October 2007; published 22 January 2008)

First-principles density functional theory was used to determine the structural properties and thermodynamic stability of strained heterojunctions between cubic SiC and hexagonal ZrB_2 films grown on Si(100) platforms. The SiC films were generated experimentally via single source depositions of the $SiH_3C{\equiv}C{-}SiH_3$ compound on ZrB_2/Si(100) hybrid substrates. In this study, a fixed stoichiometry ($Si_6C_6Zr_6B_{12}$) supercell was used to calculate the equilibrium atomic and electronic structure of six plausible bonding arrangements at the SiC/ZrB_2 interface, involving tetrahedrally coordinated C or Si centers bonded with either Zr or B atoms. The relative stability of the resultant structures is examined as a function of the Si and Zr chemical potentials. We find that the lowest energy configuration comprises of Si centers bonded to one C and three Zr atoms and exhibits the smallest bond strains with "bulklike" interatomic distances. This lowest energy structure is also consistent with cross-section transmission electron microscopy measurements of the near-interface region of SiC(111) films grown on ZrB_2(0001) buffered Si(111). A detailed analysis of the electronic structure indicates that delocalized "sheetlike" metallic bonding stabilizes this structure between covalent SiC and semimetallic ZrB_2. Assuming no intermixing at the interface, this lowest energy model suggests that the SiC overlayers *grown* on ZrB_2 are C terminated. However, calculations on isolated SiC slabs predict that Si termination is preferred, in accord with experimental observations for SiC grown on various substrates.

DOI: 10.1103/PhysRevB.77.035326 PACS number(s): 68.35.Ct, 68.35.Md, 81.15.Aa

I. INTRODUCTION

Thin films of cubic silicon carbide (3C-SiC or β-SiC) grown on Si substrates are of technological interest due to applications in various electronic and display devices. Desirable key properties that make this wide band gap semiconductor suitable for high-temperature, -power, and -frequency applications include superior thermal conductivity, enhanced saturated electron drift velocity, and high junction breakdown electric field.[1] However, the direct integration of 3C-SiC on inexpensive Si substrates is problematic due to the large mismatch ($\sim$19%) between the two materials.[2] Furthermore, the high deposition temperatures (970–1300 °C) that are required for growth of crystalline material on Si promote atomic intermixing at the interface which degrade the structural quality of the films making them unsuitable for device applications.[3,4] A practical route for the integration of cubic SiC with Si substrates is therefore highly desirable from both technological and economic points of view.

The most commonly used approach to grow epitaxial 3C-SiC on Si substrates involves the use of routes, including Si-C precursors, which enable low growth temperatures that lead to high-quality film morphology, microstructure, and compositional control.[3–5] One approach, in particular, utilizes acetylene (C_2H_2) as a reactant to introduce substitutional C atoms into the Si lattice directly at the vicinity of the substrate surface. This produces an interface layer containing C—Si bonds which are identical in length (1.90 ± 0.03 Å) to those of bulk SiC crystals. This layer serves as a nearly lattice-matched template for subsequent growth of quasiuniform SiC crystallites in the form of flat islands[5] rather than the more desirable continuous films with uniform thickness and flat surface. A second more systematic approach leading to continuous layers exploits suitable buffer layers which accommodate the structural and thermal mismatches between the film and the substrate. We recently demonstrated this approach by growing SiC films on Si(111) via conductive and reflective ZrB_2 buffer layers with a hexagonal AlB_2-type structure.[2] This represents a practical route to the integration of this material with silicon platforms and has the potential to significantly lower the cost in the conventional application of cubic SiC materials as a high-temperature optoelectronic material. In this context the ZrB_2 film serves as a reflecting intermediate layer, which prevents any loss of emission intensity from any subsequently deposited active overlayers, into the absorbing Si substrate. Very thick high-quality layers of the compound possessing low dislocation densities have recently been grown on Si(111) and this represents an important breakthrough in the integration of an entire class of tetrahedral semiconductor materials with Si technologies.[2] More fundamentally, ZrB_2 is a semimetallic compound with metalliclike reflectivity whose structural properties are in perfect analogy to the justifiably famous MgB_2 superconductor phase with the classic AlB_2 structure. Due to their unique properties the general family of MB_2 diboride compounds has attracted tremendous recent attention from both fundamental and practical viewpoints.

A preliminary theoretical account of the structure and stability in the above system was briefly described in our prior work,[2] but fundamental bonding, and electronic and structural properties were not elucidated to any significant extent.

1098-0121/2008/77(3)/035326(10)

©2008 The American Physical Society

Nevertheless, density functional theory (DFT) at the generalized gradient approximation (GGA) level was used to identify plausible interface bonding configuration based on thermodynamic considerations. Here we expand this study by analyzing the electronic properties of the most energetically favorable interfaces in detail. We employ six structural models with distinctly different interface structures and determine their corresponding energies as a function of their constituents' chemical potentials. In addition, ground state wave functions and densities are used to calculate the electron localization functions (ELFs) whose spatial topology is used to study the detailed nature and origin of the bonding within this unusual heterojunction between a semimetallic system (ZrB_2) and a prototypical covalent group IV ceramic materials (SiC).

Although the primary emphasis of the present work is on the interface behavior of the system, the surface energies of the SiC and ZrB_2 components are also obtained as a byproduct of the calculations. Since the interface slab energies are derived using the energies of independent SiC and ZrB_2 free-surface slabs, our work thus provides insight into the relative surface stability in the SiC system; the corresponding surface stabilities in the ZrB_2 system were described in our previous work.[2] In this regard, we note that the mechanism involved in the stabilization of cubic SiC on various substrate surfaces is still somewhat controversial from both fundamental and purely experimental perspectives.[6–10] For example, it has been theoretically determined that high-quality 3C films are readily stabilized in a Si-rich growth environment.[6] This is consistent with complementary experimental studies which find that the nucleation of 3C phase in (111) orientation is generally preferred under conditions involving a large Si/C-flux ratio.[7,8] However, two closely related theoretical studies of the film's terminal (111) surface appear to disagree on the relative stability of the Si and C terminations.[9,10] For our SiC(111) growth on hexagonal ZrB_2 surfaces we show that a carbon terminated film surface is energetically preferred when SiC is bonded to the Zr-terminated ZrB_2 buffer. However, calculations on isolated SiC slabs indicate that Si termination is preferred, in accord with experimental observations for SiC growth on various substrates.

We note that the inherently large (2%–3%) lattice mismatch in SiC/ZrB_2 heteroepitaxial structures required an artificial strain to be imposed on the SiC layer in order to make our simulations tractable, the so-called coherent interface approximation. To estimate the effect of this strain on our interface bonding configurations we carried out a detailed study of the epitaxial softening behavior in SiC(111) which showed that the latter film becomes stiffer under these conditions. The structurally optimized interface models also provide a detailed description of the deviations of interface bond species from their bulk values, which may be probed experimentally using surface analytical techniques such as low energy electron diffraction (LEED). The epitaxial softening calculations provide a means of correcting the artificially strained bond lengths in our model to an approximately zero-strain state.

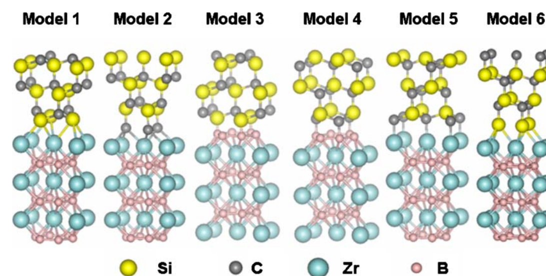

FIG. 1. (Color online) Ball and stick structural representations of the six interface configuration models considered in this study.

II. COMPUTATIONAL DETAILS AND BACKGROUND

In our preliminary work[2] we briefly described nine $Si_6C_6Zr_6B_{12}$ interface models with specific bonding arrangements between 3C—SiC(111) and ZrB_2(0001). Our present work focuses on six of the most energetically competitive models among these, denoted here by $m=1-6$. In order to accommodate the possibility of lateral reconstructions within the interface plane we adopted a supercell with a $(\sqrt{3}\times 1)$ basal dimension (3.169×5.489 Å^2) and a perpendicular length of 38 Å. The basal dimensions are derived from the bulk unit cell of the ZrB_2 buffer, and are held fixed in all structural optimizations. All supercells contain one $Si_6C_6Zr_6B_{12}$ unit, and incorporate sufficient vacuum space above and below these slabs to minimize coupling between their free surfaces. Because of the large lattice mismatch between ZrB_2 ($a_{ZrB_2}=3.169$ Å) and SiC ($d[111]=3.082$ Å) two choices emerge for making the interface calculation tractable based on the coherent interface approximation. Either the SiC can be expanded to match the dimensions of the larger ($\sim+2.8\%$) ZrB_2 lattice, or the buffer can be compressed to achieve a match with the SiC overlayer. Here we follow our prior work and adopt cell dimensions which impose a tensile strain on SiC to accommodate the stiffer and considerably thicker (bulklike) ZrB_2 template employed in our experiments. We further assume that the large strain differential associated with this coherent interface approximation does not alter the energetic ordering of the interfacial bonding arrangements. The six models treated in the present work are described in Fig. 1 and comprise a range of chemically distinct interface configurations containing bonds between Zr—Si (models 1 and 6), Zr—C (models 2 and 5), B—Si (model 3), and B—C (model 4).

Unless otherwise specified, all electronic and atomic structure calculations of the SiC(111)-ZrB_2(0001) heterojunction were carried out using the Vienna *ab initio* simulation package (VASP).[11–13] This program employs pseudopotentials derived from the projected augmented wave formalism[14] and the PW91 form of the GGA functional.[15] A plane wave cutoff energy of 400 eV was used in conjunction with a $7\times 4\times 1$ Monkhorst-Pack grid to achieve a force accuracy of 0.01 eV/Å. Using these computational parameters, the atomic coordinates were fully relaxed to their zero force positions, yielding optimized atomic structures. The calculation of the interface energy, Γ, used in the present work follows closely our approach described in Ref. 2 and is based

on the use of free-surface-terminated slabs comprised of two approximately equal multilayer units of pure SiC and ZrB_2. The entire slab is repeated in space in the direction normal to the interface, and the cross-sectional area (as described above) is fixed in all calculations. The total energy of the combined SiC-ZrB_2 slab, $E_{slab}^{\mathrm{SiC/ZrB_2}}$, is then given by the following equation:

$$E_{slab}^{\mathrm{SiC/ZrB_2}} = n_{\mathrm{Si}}\mu_{\mathrm{Si}} + n_{\mathrm{C}}\mu_{\mathrm{C}} + n_{\mathrm{Zr}}\mu_{\mathrm{Zr}} + n_{\mathrm{B}}\mu_{\mathrm{B}} + A(\sigma^{\mathrm{SiC}} + \sigma^{\mathrm{ZrB_2}}) + A\Gamma_m, \quad (1)$$

where Γ_m is the interface energy of the specific SiC—ZrB_2 bonding model m, and A is the cross-sectional surface area. The number of atoms of Si, C, Zr, and B are given by n_{Si}, n_{C}, n_{Zr}, and n_{B}, respectively, while the corresponding chemical potentials are denoted by μ_{Si}, μ_{C}, μ_{Zr}, and μ_{B}. Finally, the surface energies of SiC and ZrB_2 are denoted by σ^{SiC} and $\sigma^{\mathrm{ZrB_2}}$, respectively.

III. CHEMICAL POTENTIALS

Equation (1) indicates that once the slab energies and surface formation energies σ are supplied, the interface energies of interest in this study, Γ_m, are thermodynamic functions of the chemical potentials μ of the constituent atoms in the slab. Therefore, the interface energy depends on the chemical potentials (μ_{Si}, μ_{C}, μ_{Zr}, and μ_{B}) and this dependence can be further simplified by eliminating μ_{C} and μ_{B} in favor of μ_{Si} and μ_{Zr} using the bulk thermodynamic equilibrium conditions

$$\mu_{\mathrm{Si}} + \mu_{\mathrm{C}} = \mu_{\mathrm{SiC}}^{bulk}, \quad (2)$$

$$\mu_{\mathrm{Zr}} + 2\mu_{\mathrm{B}} = \mu_{\mathrm{ZrB_2}}^{bulk}. \quad (3)$$

At a surface or an interface, the chemical potentials of Si and Zr are restricted within the thermodynamically allowed ranges determined by the corresponding bulk phases of Si and Zr, and the alloys SiC and ZrB_2,[16] as follows:

$$\mu_{\mathrm{Si}}^{bulk} + \Delta H^f[\mathrm{SiC}] \leqslant \mu_{\mathrm{Si}} \leqslant \mu_{\mathrm{Si}}^{bulk} \quad (4)$$

and

$$\mu_{\mathrm{Zr}}^{bulk} + \Delta H^f[\mathrm{ZrB_2}] \leqslant \mu_{\mathrm{Zr}} \leqslant \mu_{\mathrm{Zr}}^{bulk}, \quad (5)$$

where the formation enthalpies of bulk SiC and ZrB_2 are given by

$$\Delta H^f[\mathrm{SiC}] = \mu_{\mathrm{SiC}}^{bulk} - \mu_{\mathrm{Si}}^{bulk} - \mu_{\mathrm{C}}^{bulk} = -0.542 \text{ eV}, \quad (6)$$

$$\Delta H^f[\mathrm{ZrB_2}] = \mu_{\mathrm{ZrB_2}}^{bulk} - \mu_{\mathrm{Zr}}^{bulk} - 2\mu_{\mathrm{B}}^{bulk} = -2.952 \text{ eV}. \quad (7)$$

The bulk chemical potentials μ_i^{bulk} are determined from the total energies per atom of elemental Si, C, Zr, and B and the corresponding alloys SiC and ZrB_2, in their standard room temperature solid forms as listed in Table I. Note that our calculated ΔH values are very similar to other available GGA estimates: $\Delta H^f[\mathrm{SiC}]=-0.580$ eV and $\Delta H^f[\mathrm{ZrB_2}]=-3.076$ eV.[17,18] Finally, substitution of Eqs. (6) and (7) into Eqs. (4) and (5) yields $-0.542\text{ eV} \leqslant \mu_{\mathrm{Si}} - \mu_{\mathrm{Si}}^{bulk} \leqslant 0$ and $-2.952\text{ eV} \leqslant \mu_{\mathrm{Zr}} - \mu_{\mathrm{Zr}}^{bulk} \leqslant 0$, or simply $-0.542\text{ eV} \leqslant \Delta\mu_{\mathrm{Si}} \leqslant 0$ and $-2.952\text{ eV} \leqslant \Delta\mu_{\mathrm{Zr}} \leqslant 0$ where $\Delta\mu_i = \mu_i - \mu_i^{bulk}$. The latter chemical potential designations are then used throughout the rest of our discussion.

TABLE I. Ground state phase used to compute the bulk chemical potentials and formation energies of the elemental constituents Si, C, Zr, and B and the alloys SiC and ZrB_2.

	Structure	μ_i (eV)	ΔH^f (eV)
Si	$Fd\underline{3}m$	−5.42	
C	$P6_3/mmc$	−9.10	
SiC	$F43m$	−15.06	−0.542
Zr	$P6_3/mmc$	−8.42	
B	$R3m$	−6.68	
ZrB_2	$P6/mmm$	−24.72	−2.952

IV. SURFACE ENERGIES

The conventional approach to calculating the surface energy involves the independent determination of the energy per unit cell of an n-layer slab, E_n, and bulk energy, E_B, of a corresponding infinite solid, from which $\sigma = \lim_{n\to\infty}\frac{1}{2}(E_n - nE_B)$. For finite slabs (ultrathin films) Boettger demonstrated that small differences between the bulk energies derived in the context of a slab and the bulk solid can lead to significant errors in the determination of surface energy.[19] We therefore adopt Boettger's approach in the present work, from which the total energies between two slabs of different thickness are given by

$$\sum_i n_i \mu_i = E_n - E_{n-a}, \quad (8)$$

where n_i and μ_i are the number of atoms and the chemical potential of the ith constituent of the slab. E_n and E_{n-a} are the energies per unit cell of the n and $n-a$ layer slabs, where $n > a$. Thus, to calculate the various possible bonding arrangements at the interface we consider both Si- and C-terminated ordering to obtain surface energies required for the SiC slab. An identical procedure is applied to the surface energy calculations of ZrB_2. In this study these energies are obtained from accurate independent calculations based on thick 11- and 5-layer slabs (Fig. 2). Note that here the odd number of layers ensures that the chemical termination on both sides of the slab is the same. The bulk energies for the slabs with repeated geometry are then given by the equations

$$E_{slab}^{\mathrm{SiC}} = n_{\mathrm{Si}}\mu_{\mathrm{Si}} + n_{\mathrm{C}}\mu_{\mathrm{C}} = E_{11}^{\mathrm{SiC}} - E_5^{\mathrm{SiC}} \quad (9)$$

and

$$E_{slab}^{\mathrm{ZrB_2}} = n_{\mathrm{Zr}}\mu_{\mathrm{Zr}} + n_{\mathrm{B}}\mu_{\mathrm{B}} = E_{11}^{\mathrm{ZrB_2}} - E_5^{\mathrm{ZrB_2}}. \quad (10)$$

Subtracting Eqs. (9) and (10) from Eq. (1) we obtain

$$\Delta E_{slab} = E_{slab}^{\mathrm{SiC/ZrB_2}} - E_{slab}^{\mathrm{SiC}} - E_{slab}^{\mathrm{ZrB_2}}. \quad (11)$$

Here ΔE_{slab} approximates the negative of the work of adhesion, W_a, between isolated SiC and ZrB_2 slabs with free sur-

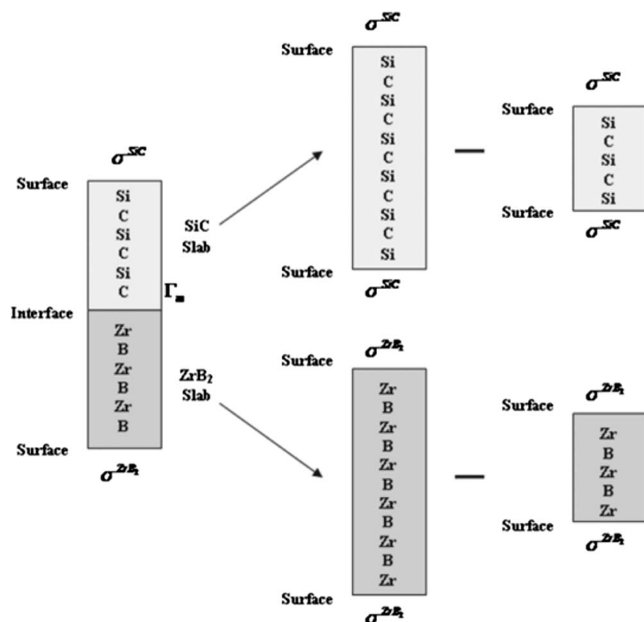

FIG. 2. Schematic illustration of the layer compositions within the various slabs employed in our calculations: Left panel: joined SiC/ZrB_2 slab with an even number of Si-C and $Zr-B_2$ layers corresponding to a fixed stoichiometry (see text). Center and right panels illustrate the particular choice of Si-terminated SiC and Zr-terminated ZrB_2 slabs with 11 and 5 layers, respectively.

faces, and is related to the interface energy, Γ_m, by the equation

$$\Gamma_m = \Delta E_{slab}/A\sigma^{\text{SiC}} - \sigma^{\text{ZrB}_2}. \quad (12)$$

The basic approach used here is therefore similar to that employed in our previous work on GaN/ZrB_2 interfaces;[20] however, here we apply a more accurate procedure to the calculation of surface energies in the SiC/ZrB_2 system.

All of our SiC and ZrB_2 surfaces are modeled using repeated slab geometries in which the dangling bonds at the surface of slabs are separated by a vacuum region approximately 20–30 Å thick. The surface formation energies, σ, can be expressed by the following equation:

$$\sigma = \left(E_{\text{slab}} - \sum_i n_i\mu_i\right) \Big/ (2A), \quad (13)$$

where E_{slab} is the total energy of the particular slab, and the μ_i's are obtained from the Boettger procedure described above. This differs from the approach used in our earlier work[2] where the μ_i values were approximated using infinite bulk solid calculations. The factor of 2 in Eq. (13) accounts for the fact that the separated slabs each contain two equivalent surfaces, as shown in the center and right panels of Fig. 2. Also note that while Fig. 2 shows Si-terminated SiC and Zr-terminated ZrB_2 slabs with 11 and 5 layers, respectively, identical calculations were conducted to obtain the corresponding surface energies of C- and B-terminated slabs of SiC and ZrB_2.

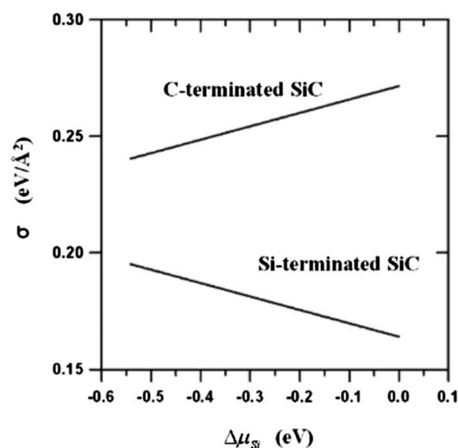

FIG. 3. Comparison of Si- and C-terminated SiC(111) surface energies σ as a function of $\Delta\mu_{\text{Si}}$.

In our prior work in the GaN/ZrB_2 system the coherent interface approximation was fully justified on the basis of the small lattice mismatch between GaN and ZrB_2.[20] Here this approximation imposes rather large artificial tensile strains in the SiC component and thus the surface energies obtained using the above procedure should not be directly compared with those of a relaxed system. Below we describe corrections to the bond lengths based on the epitaxial softening behavior of SiC under large finite strains. Nevertheless, in the context of the present work we shall assume that the strain introduced by our coherent interface treatment does not alter the energetic ordering of the interface models. The validity of this assumption could in principle be verified *a posteriori* by repeating our study for the case in which the ZrB_2 is compressed to match the dimensions of a relaxed SiC overlayer. As mentioned above the basal lattice dimensions of all SiC/ZrB_2 $(1\times\sqrt{3})$ supercells are therefore fixed at $a=3.169$ Å and $b=5.489$ Å. With this constraint, all atomic positions are allowed to relax fully within each supercell of fixed dimensions in each of the structural models corresponding to the joined slab, yielding $E_{slab}^{\text{SiC/ZrB}_2}$.

The surface energy of $ZrB_2(0001)$ versus $\Delta\mu_{\text{Zr}}$ in the range $-2.952\text{ eV}\leqslant\Delta\mu_{\text{Zr}}\leqslant 0$ has been discussed in our previous work for the related GaN/ZrB_2 epitaxial system, where we showed that the Zr-terminated $ZrB_2(0001)$ surface is more stable than its B-terminated counterpart over the entire range of allowed $\Delta\mu_{\text{Zr}}$ values.[20] Here we calculate the surface energies of σ^{SiC} by following a similar procedure for $\Delta\mu_{\text{Si}}$ in the thermodynamically allowed range $-0.542\text{ eV}\leqslant\Delta\mu_{\text{Si}}\leqslant 0$. The end values of the $\Delta\mu_{\text{Si}}$ parameter, −0.542 and 0 eV, correspond to Si- and C-rich conditions, respectively. A plot of the surface energy of SiC versus $\Delta\mu_{\text{Si}}$ is shown in Fig. 3 and indicates that the Si-terminated 3C-SiC(111) surface is the more stable one over the entire range of allowed chemical potentials. Our result in Fig. 3 agrees with other first-principles calculations of Si-rich surface reconstruction for 3C-SiC(111) films grown on SiC substrates,[6] and corroborates the experimental reflection high energy electron diffraction results for Si-covered 3C-SiC(111)/SiC surfaces.[21]

V. INTERFACE ENERGIES AND STRUCTURES

The SiC/ZrB_2 interface energy, Γ, as defined by Eq. (12), is a bilinear function of the chemical potentials $\Delta\mu_{Si}$ and $\Delta\mu_{Zr}$. To compare the thermodynamic stability of the six interface models depicted in Fig. 1, we constructed three-dimensional (3D) plots of Γ_m (where $m=1-6$) versus $\Delta\mu_{Si}$ and $\Delta\mu_{Zr}$ for all six models as shown in Fig. 4. Specifically, the atomic structures of the interfaces include two types each of Si—Zr bonding arrangements (models 1 and 6), two types each of C—Zr bonding interfaces (models 2 and 5), and one type each of Si—B bonded (model 3) and C—B bonded (model 4) systems. From Fig. 4, it can be seen that model 6 is predicted to be the most stable under Zr-rich conditions, with an interface structure consisting of tetrahedrally coordinated Si, i.e., one Si—C bond and three Si—Zr bonds. To further clarify the behavior described in Fig. 4 we also present two-dimensional plots of the interface energy in Figs. 5(a)–5(d), for fixed values of chemical potentials corresponding to $\Delta\mu_{Si}=0$ (Si rich), $\Delta\mu_{Si}=-0.542$ eV (C rich), $\Delta\mu_{Zr}=0$ (Zr rich), and $\Delta\mu_{Zr}=-2.952$ eV (B rich), respectively.

It can be observed in Figs. 5(a) and 5(c) that the interface energy Γ_6 of model 6 has the lowest energy of −0.015 eV in

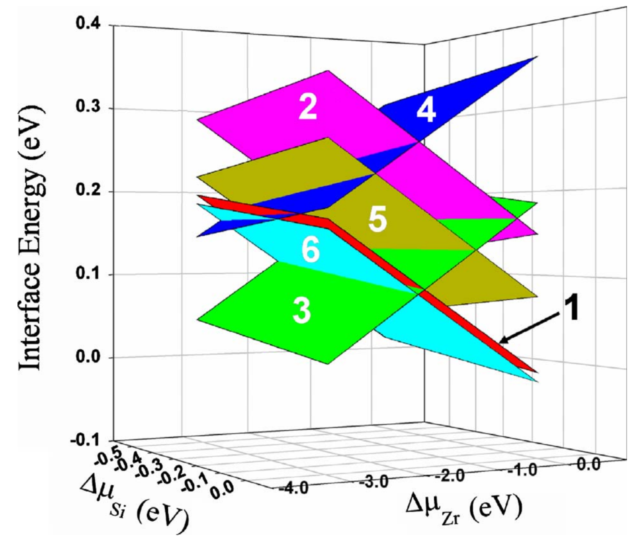

FIG. 4. (Color online) 3D plot of interface energies of the six SiC/ZrB_2 models as bilinear functions of the allowed Si and Zr chemical potentials, $\Delta\mu$. Model 6 has the lowest interface energy among all six models.

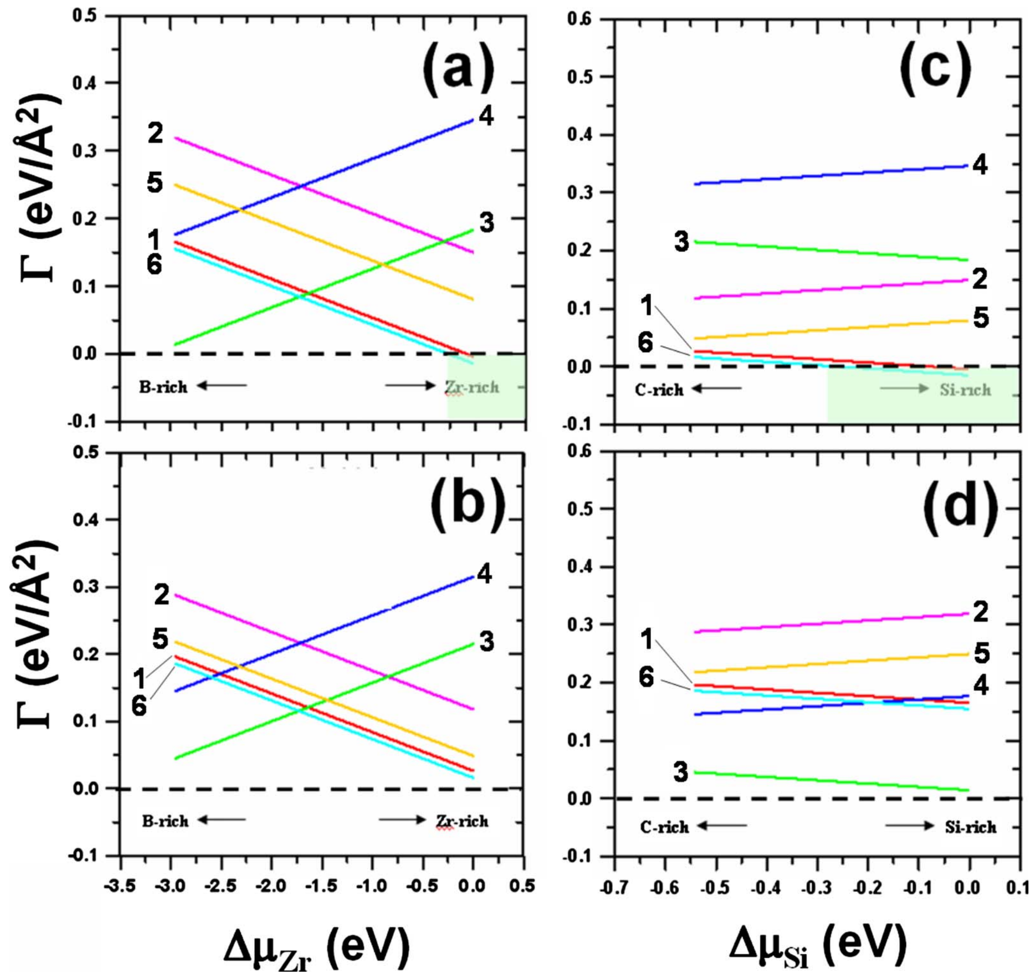

FIG. 5. (Color online) Two-dimensional plots of the interface energy corresponding to (a) $\Delta\mu_{Si}=0$ (Si rich), (b) $\Delta\mu_{Si}=-0.542$ eV (C rich), (c) $\Delta\mu_{Zr}=0$ (Zr rich), and (d) $\Delta\mu_{Zr}=-2.952$ eV (B rich), respectively.

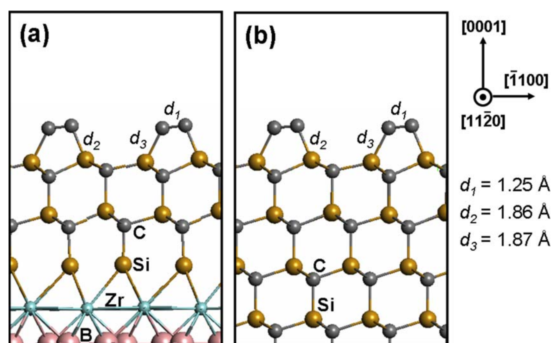

FIG. 6. (Color online) Reconstruction of the C-terminated surfaces of (a) SiC/ZrB_2 model 6 structure and (b) 11-layer SiC slab. The C═C dimers are approximately parallel to the surface (as shown above), with their bond axis directed along the $[\bar{1}2\bar{1}0]$ direction.

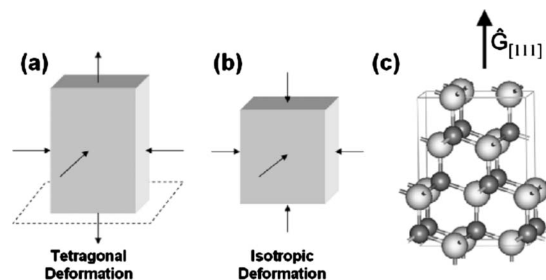

FIG. 7. Schematic illustration showing the geometric relationship between a tetragonally (a) and isotropically (b) distorted structure. (c) The orthorhombic cell representation of cubic SiC, shown in relation to the orientational vector $\hat{G}_{[111]}$ corresponding to the growth direction (large and small spheres are Si and C, respectively).

the Si-rich and Zr-rich limits, i.e., at $\Delta\mu_{Si}=0$ and $\Delta\mu_{Zr}=0$. This corresponds to a Si-Zr interface and a C-terminated 3C-SiC(111) surface as depicted in model 6 in Fig. 1. Apart from model 6, the only other interface that exhibits stability is model 1 in the Si-rich and Zr-rich limits, i.e., at $\Delta\mu_{Si}=0$ and $\Delta\mu_{Zr}=0$, where $\Gamma_1=-0.005$ eV as shown in Figs. 5(a) and 5(c). This corresponds to a Si-Zr interface and a C-terminated 3C-SiC(111) surface as shown in model 1. The stability fields for the formation of the interfaces in models 1 and 6 are denoted by the shaded region in Figs. 5(a) and 5(c). However, it should be noted that in these regions of $\Delta\mu_{Si}$ and $\Delta\mu_{Zr}$ associated with Si-rich and Zr-rich conditions model 6 has the overall lowest interface energy. This implies that growth of 3C-SiC on ZrB_2 will result in a Si-Zr interface and a C-terminated 3C-SiC(111) surface under the Si-rich and Zr-rich conditions. This basic result was described in our prior work where we also carried out a detailed comparison of the interface structure predicted by our simulations with experimental transmission electron microscopy (TEM) micrographs of the SiC/ZrB_2 interface region on an atomic scale.[2] The data indicate that the structure of lowest energy model (model 6) is, in fact, the one observed experimentally.

To elucidate the preference of the energetic trends with respect to Si bonding in the interface that leads to the C termination of the SiC layer we also examined the structure of the free surfaces of model 6. As shown in Fig. 6 the C-terminated surface of the SiC/ZrB_2 interface model 6 undergoes a dimer reconstruction which is virtually identical to that found on the free C-terminated surface of our 11-layer SiC slabs. This energy lowering mechanism for the free C-terminated surfaces is thus inherently included in our description. In both cases the calculated dimer and surface Si—C bond lengths are 1.25 and ~1.87 Å, respectively, in excellent agreement with the corresponding observed values, 1.25–1.32 and 1.85–1.93 Å, determined from LEED measurements.[22]

VI. EPITAXIAL STABILIZATION OF 3C-SiC(111) FILM

To elucidate the energetic and structural effects associated with the use of the coherent interface approximation we carried out a brief comparative study of the epitaxial stabilization behavior in the SiC and Si systems. Here the coherent confinement of the epilayer's lattice constant by the substrate leads to a structural relaxation along a direction $\hat{G}$ normal to the interface. The energy lowering associated with this process is called "epitaxial stabilization" and is illustrated in Fig. 7 for the most common example of a tetragonally deformed system and its isotropically compressed counterpart. The epitaxial softening associated with these strain film states can be quantified by the dimensionless parameter q defined by[23]

$$q(a_f,\hat{G}) = \Delta E^{epi}(a_f,\hat{G})/\Delta E^{bulk}(a_f). \quad (14)$$

This parameter represents the ratio between the increase in epitaxial energy ΔE^{epi} due to biaxial deformation to an in-plane lattice dimension a_f, and the corresponding increase in the hydrostatic energy ΔE^{bulk} due to isotropic deformation to the same value a_f. It should be noted that $a_f=a_0$ corresponds to a fully relaxed system where a_0 is the equilibrium lattice constant. In the present model the lattice orientation for the epitaxy of SiC with [111] normal to the growth plane is shown in Fig. 7(c) where an orthorhombic representation containing 6 f.u. of SiC has been adopted.

For each value of finite strain in this range we fully relaxed the supercell dimension in the [111] direction, and all internal atomic positions to the zero stress and zero force values, respectively. Reciprocal space integrations were carried out using 40 irreducible k points generated from a $2\times4\times7$ Monkhorst-Pack grid in the first Brillouin zone. With these parameters and a plane wave cutoff of 400 eV we obtained relaxed lattice constants $a=3.091$ Å, $b=5.358$ Å, and $c=7.575$ Å for the equilibrium structure. The associated energy was then used as a reference for the epitaxial deformation calculations. The top panels of Fig. 8 compare the energy-strain relationship for hydrostatically and epitaxially strained SiC and Si over the wide strain range from −3% to 3%. At the largest tensile strain value of +3%, our calculations indicate that epitaxy lowers the energy of SiC by ~20 meV/f.u. compared to the hydrostatically compressed reference state. The corresponding value for silicon at +3% strain is only ~16 meV, indicating that SiC is significantly

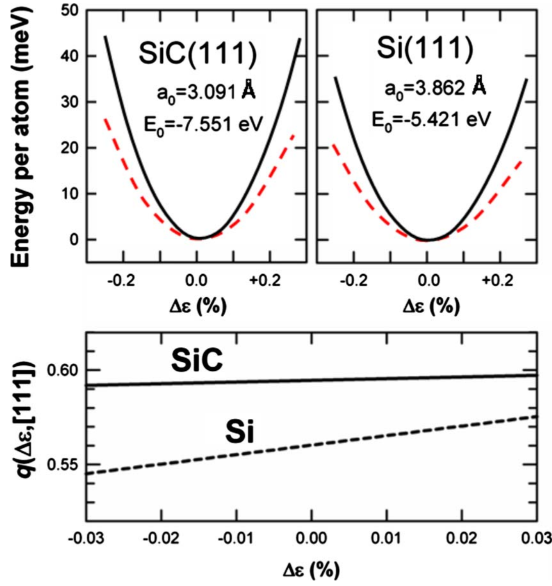

FIG. 8. (Color online) Top panels: bulk (solid line) and epitaxial (dashed line) strain energies for SiC(111) and Si(111) as a function of basal strain. Bottom panel: epitaxial softening function for SiC(111) and Si(111) indicating that the SiC film is more anharmonic (larger value at zero strain). Both solids become stiffer on dilation (positive slopes), but the effect is significantly smaller in SiC.

stiffer than Si even in a film state. This is corroborated by a plot of the epitaxial softening function $q(a_f,[111])$, as defined in Eq. (14), in the bottom panel of Fig. 8 which shows that both SiC and Si become stiffer upon dilation (tensile strain). However, the data also indicate that SiC possesses a slightly larger value of $q(a_0,[111])$ at the equilibrium lattice constant a_0, indicating that it is more elastically anharmonic than Si.

In our prior work[2] we demonstrated by explicit comparisons with atomic structures derived from experimental cross-section TEM (XTEM) micrographs that models 1 and 6 represent plausible interface bonding configurations. It is therefore also of significant interest to carry out a detailed comparison of the bond lengths in these models with those obtained from other experimental and theoretical studies. Our interface structure simulations also yield information about the distribution of bonds near the heterojunction. In this regard, model 6 (the most energetically favored model) yields a Si—Zr bond length of 2.79 Å which closely matches the value 2.9 Å found experimentally in Zr-encapsulated caged clusters of silicon.[24] This is also similar in value to bond lengths 2.66 Å found in simulation studies of Zr-silicate/silicon interfaces.[25] By contrast, the Si—Zr bond length of 3.09 Å in model 1 (second most favorable) is approximately 11% longer than in model 6 indicating a weaker bond in the less stable model.

Further insight into the origin of the interface stability can be obtained by examining the deviations of the bond length adjacent to the heterojunction from their bulk values. The latter bond lengths are calculated from optimized unit cells of the bulk SiC and ZrB_2 crystals (a_{SiC}=4.37 Å, a_{ZrB_2}=3.17 Å, and c_{ZrB_2}=3.55 Å, respectively). Table II lists the results of our bond length analysis for models 1 and 6. For the most favorable interface geometry (model 6) the Si—C and Zr—B bond lengths immediately adjacent to the interface layer are slightly compressed relative to their bulk values, while the corresponding bond lengths in the more distant second layers on either side of the interface are slightly expanded. The data indicate that the largest bond relaxations occur in the first layer of ZrB_2 (−0.89%) and the second layer of SiC (2.11%). The corresponding trends in model 1 are similar except that the bond length in the first layer of SiC exhibits a larger *positive* deviation from its bulk value. Overall, the magnitude of the deviations in model 1 is larger suggesting a less favorable bonding arrangement within the interface region. The more bulklike bond length distributions in model 6 are consistent with its lower energy.

Finally, as noted earlier in our discussion, the effect of the artificial strain must be taken into account in any direct comparisons between the interface and/or surface bonds in the SiC/ZrB_2 presented here and experimental data. In tetrahedrally bonded solids with a positive Poisson ratio tensile strain in the interface plane leads to a contraction of the bonding in the normal direction. In the limit of small distortions the strains parallel and perpendicular to [111] in a cubic system are related by harmonic elastic theory according to $\varepsilon_\perp/\varepsilon_\parallel=-2(2C_{11}+2C_{12}-C_{44})/(C_{11}+2C_{12}+2C_{44})$, where the C_{ij}'s are 3C-SiC elastic constants (C_{11}=390 GPa, C_{12}=142 GPa, and C_{44}=256 GPa). For the large finite strain $\varepsilon_\parallel \sim +2.81\%$ imposed in our SiC slab models this simple estimate predicts a perpendicular strain (contraction) of $\varepsilon_\perp \sim -3.8\%$ which differs significantly from the value $\varepsilon_\perp \sim -2.85\%$ obtained from our epitaxial softening calculations. The 3C—SiC bond lengths perpendicular to the SiC/ZrB_2 interface in a fully relaxed SiC film can thus be estimated from our calculated values dilating the latter by ∼3%–4%.

TABLE II. Percent deviations of near-interface bond lengths from their corresponding bulk values for models 1 and 6. The superscripts "1" and "2" in the ratios $\Delta d/d$ denote bond lengths within the first and second layers on either side of the interface. $\Delta d^1_{Si—C}/d^{bulk}_{Si—C}$, $d^2_{Si—C}/d^{bulk}_{Si—C}$, $\Delta d^1_{Zr—B}/d^{bulk}_{Zr—B}$, and $\Delta d^2_{Zr—B}/d^{bulk}_{Zr—B}$ for the 3C—SiC(111)—ZrB_2(0001) interfaces of models 1 and 6. $\Delta d^1_{Si—C}$, $\Delta d^2_{Si—C}$, $\Delta d^1_{Zr—B}$, and $\Delta d^2_{Zr—B}$ are the innermost and second Si—C and Zr—B bond lengths respectively.

	$\Delta d^1_{Si—C}/d^{bulk}_{Si—C}$	$\Delta d^2_{Si—C}/d^{bulk}_{Si—C}$	$\Delta d^1_{Zr—B}/d^{bulk}_{Zr—B}$	$\Delta d^2_{Zr—B}/d^{bulk}_{Zr—B}$
Model 1	2.50%	2.85%	−1.65%	0.24%
Model 2	−0.04%	2.11%	−0.89%	0.37%

VII. ELECTRONIC PROPERTIES OF THE INTERFACE

The energetic stability of the various SiC/ZrB_2 interface configurations is intimately related to their respective electronic bonding properties. A common approach adopted in many studies is to analyze the electronic charge density, $\rho(\mathbf{r})$, or its deviation, $\Delta\rho(\mathbf{r})$, from a reference state such as the superposition of constituent neutral atoms. This is arguably an arbitrary choice which can lead to difficulties in interpretation depending on the specific bonding character of the target system (e.g., covalent, ionic, and semimetallic). In our particular case of the SiC/ZrB_2 system, the covalent (SiC) and semimetallic (ZrB_2) character within the bulk materials is manifestly different and in this regard the nature of bonding at the interface is not obvious, and must therefore be analyzed using a methodology which is unambiguous. Here we adopt the ELF because of its ability to systematically identify distinct types of bonding behavior based only on spatial distributions obtained from DFT densities and wave functions.

A useful and practical definition of the electron localization function in terms of the ground state Kohn-Sham orbitals and corresponding density was introduced by Silvi and Savin[26] who introduced the form $\mathrm{ELF}=[1+(D/D_h)^2]^{-1}$, where the "excess" kinetic energy is defined by $D=\frac{\hbar^2}{2m}\Sigma_i|\nabla\varphi_i(\vec{r})|^2-\frac{\hbar^2}{8m}\frac{|\nabla\rho(\vec{r})|^2}{\rho(\vec{r})}$ and the homogeneous electron gas contribution is $D_h=\frac{3}{5}\frac{\hbar^2}{2m}(3\pi^2)^{2/3}\rho^{5/3}$. In our study the orbitals $\varphi_i(\vec{r})$ and corresponding density $\rho(\vec{r})$ are exclusively valence electron quantities obtained using the GGA within a plane wave basis. From this definition of the ELF it can be readily noted that $D/D_h\sim 1$ in regions where the density gradients vanish yielding an ELF of 0.5. On the other hand, electron localization is enhanced in regions where excess kinetic energy is small, $\frac{\hbar^2}{2m}\Sigma_i|\nabla\varphi_i(\vec{r})|^2\approx\frac{\hbar^2}{8m}\frac{|\nabla\rho(\vec{r})|^2}{\rho(\vec{r})}$, leading to $\mathrm{ELF}\sim 1$. Electron localization function values in the range 0–0.5 are found in areas of low electron density. Thus the ELF ranges in value from 0 to 1 and its isosurfaces roughly mimic the classical Lewis description of bonding thereby providing a very systematic spatial picture of bonding and nonbonding electron pairs. The spatial distribution of bonding and nonbonding ELF patterns has been studied by Becke and Edgecombe[27] who introduced the concept of "attractors" and described their usefulness in the systematic classification of bonds based on the topology of the ELF. These concepts have also recently been used to analyze the bonding and nonbonding behaviors near semiconductor surfaces.[28]

Here we use the electron localization function to study the bonding character within the 3C-SiC(111)/ZrB_2(0001) interface. The ELF maps were calculated as two-dimensional contours within the 3.169×5.489 Å^2 interface unit cell, at five equally spaced vertical positions within the interface region, as shown in Fig. 9. This region is defined as the space between the terminal SiC or ZrB_2 atomic rows adjacent to the interface plane. Although we have generated ELF distributions for all six models, here we describe the ELFs for the two lowest energy interface configurations (models 1 and 6). We note that the width of the interface region for the lowest energy model 6 is 2.12 Å while that of the competitive analog model 1 is 2.50 Å. The vertical spacing of the panels in Fig. 9 for model 1 (A_1–E_1) and model 6 (A_6–E_6) are therefore slightly different, and this fact should be taken into account in interpreting the full three-dimensional distribution (see below).

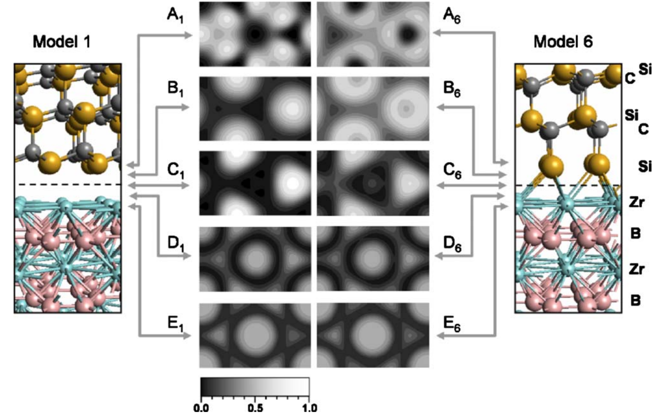

FIG. 9. (Color online) Electron localization function maps of the interface regions of models 1 and 6. The vertical position of the A and E panels coincide with the Si (gold spheres) and Zr (blue spheres) atomic planes adjacent to the interface, respectively. The dashed lines indicate the midpoint positions within each interface, and the corresponding ELF maps are labeled as C_1 and C_6. The 0–1 range of the ELF values is described by the gray scale bar at the bottom of the figure.

In the ELF map of the silicon layer adjacent to the interface in model 1 (panel A_1 in Fig. 9), the localization of bond charge toward the three nearest-neighbor C atoms is clearly indicated by the high ELF values (white). The bright regions arise from the intersection of the Si—C bond charge pockets with the A_1 plane (Si layer). The corresponding behavior in model 6 is shown as panel A_6 in Fig. 8, and indicates the onset of electron delocalization in the direction of the Zr atoms in the ZrB_2 substrate surface. This becomes even more evident in panel B_6, where the delocalization is clearly indicated by the development of lower ELF values directly below the Si atoms. In contrast the map in B_1 (model 1) shows that the corresponding electron distribution remains strongly localized. Panels C_1 and C_6 illustrate the ELF distributions at the midpoint of the two interface models. While the ELF distribution in model 1 remains well localized (values close to 1) its counterpart in model 6 displays an almost itinerant electron behavior indicated by continuous contours with values near $\sim$0.5. We note that in the proximity of the Zr layers (panels D_1–E_1 and D_6–E_6) the ELF maps in both models are virtually identical. A detailed examination of ELF maps within the near-surface ZrB_2 region indicates that this model independence persists over the entire 0–1 range.

To further elucidate the unexpected itinerant behavior in the model 6 interface structure we have plotted ELF isovalues in three dimensions and superimposed the resulting maps onto our atomic "ball and stick" models, as shown in Fig. 9. In Fig. 9(a) it can be clearly seen that a continuous distribution of $\mathrm{ELF}\sim 0.5$ exists in the interface region of model 6 (right panel) indicating sheetlike metallic bonding. This be-

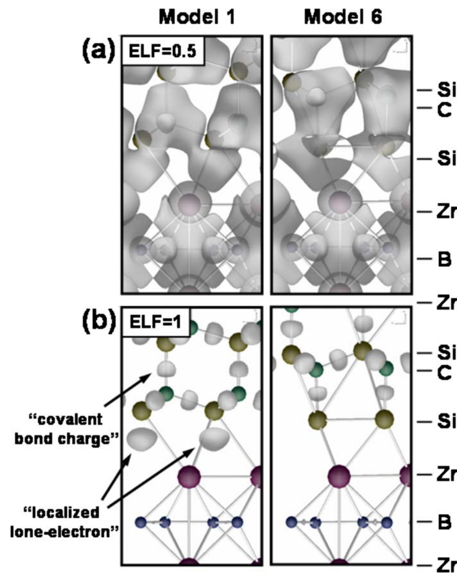

FIG. 10. (Color online) Comparison of ELF isosurfaces in models 1 and 6 for: (a) ELF=0.5 corresponding to metalliclike bonding and (b) ELF=1 which indicates the location of localized covalent bonds, and lone-electron distributions within the interface region.

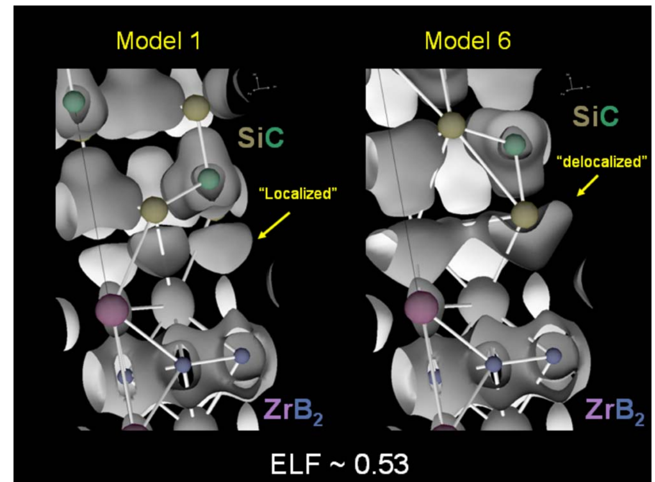

FIG. 11. (Color online) Comparison of ELF ~ 0.53 plots for models 1 and 6 emphasizing the difference in the lobe connectivity in the interface region.

havior is not as clearly obvious in the isovalue map of model 1 (left panel). Note also that above and below the midpoint of the interface within the SiC and ZrB_2 regions, for both models, the individual ELF "lobes" do not overlap indicating the absence of this metallic-type behavior. Nevertheless, a careful examination of the ELF maps in the bulk region of the ZrB_2 component reveals the presence of extended lobes which touch but do not overlap in prototypical metallic fashion. This is consistent with the inherent *semimetallic* character that bulk ZrB_2 is known to exhibit.

Our 3D ELF maps also corroborate the localized bonding at the interface as described by our two-dimensional maps in Fig. 8. In the case of model 1, the localized lone-electron lobes within the interface midpoint region become clearly visible, as shown in the left panel of Fig. 10(b). Note the absence of these high energy distributions in model 6, which is consistent with the delocalization of the charge discussed above in the context of the metallic bonding behavior. The 3D ELF maps in Fig. 10 also shed light on the bonding behavior within the first few SiC and ZrB_2 atomic layers above and below the interface. For instance, Fig. 10(b) shows a ubiquitous distribution of localized "bond charge" pockets within the prototypically covalent SiC network. Finally, Fig. 11 shows plots of the ELF ~ 0.53 values at a slightly adjusted view angle, which emphasize the differences in the lobe connectivity within the interface plane for models 1 and 6.

VIII. CONCLUSIONS

The surface and interface energies of cubic SiC(111) grown epitaxially on hexagonal $ZrB_2(0001)$ were investigated by first-principles DFT-GGA calculations. The thermodynamic stability of six relaxed interface structural models with fixed $Si_6C_6Zr_6B_{12}$ stoichiometry was analyzed and lowest energy configuration was found to be comprised of Si centers bonded to one C and three Zr atoms. This bonding structure also exhibits the smallest bond strains with bulklike interatomic distances, among the models considered. This model yields a structure which is consistent with recent XTEM observations of the near-interface atomic structure of 3C-SiC(111) films grown on $ZrB_2(0001)$.[2] Analysis of 3D ELF maps suggests that the stability of model 6 is associated with metalliclike bonding localized to the interface plane, while less energetically favorable configurations were found to involve higher energy lone-electron distributions within the interface layer. Surface energies for isolated SiC and ZrB_2 slabs were also generated in the course of our interface studies. Our results for independent SiC slabs show that a Si-terminated 3C-SiC(111) surface is energetically more favorable than its C-terminated counterpart by 50–100 meV over the accessible Si chemical range ($-0.542\text{ eV} \leq \Delta\mu_{Si} \leq 0$). However, this preference for Si termination is overcome in our model 6 interface. In this case the initial SiC/ZrB_2 bonding on the SiC side of the interface begins with a silicon layer thereby conferring C termination at the free surface of the stoichiometric film.

ACKNOWLEDGMENTS

This work was supported by the Science Foundation of Arizona, the National Science Foundation (EEC-0438400), and in part by the Ministry of Education, Taiwan, R.O.C. under the ATU plan. Computational studies were performed using the resources of the Fulton High Performance Computing Initiative at Arizona State University.

[1] P. Das and D. K. Ferry, Solid-State Electron. **19**, 851 (1976).
[2] R. Trivedi, P.-L. Liu, R. Roucka, J. Tolle, A. V. G. Chizmeshya, I. S. T. Tsong, and J. Kouvetakis, Chem. Mater. **17**, 4647 (2005).
[3] C. H. Wu, C. Jacob, X. J. Ning, S. Nishino, and P. Pirouz, J. Cryst. Growth **158**, 480 (1996).
[4] J. H. Boo, K. S. Yu, M. Lee, and Y. Kim, Appl. Phys. Lett. **66**, 3486 (1995).
[5] M. De Crescenzi, R. Bernardini, R. Gunnella, and P. Castrucci, Solid State Commun. **123**, 27 (2002).
[6] M. C. Righi, C. A. Pignedoli, R. Di Felice, C. M. Bertoni, and A. Catellani, Phys. Rev. Lett. **91**, 136101 (2003).
[7] M. Omori, H. Takei, and T. Fukuda, Jpn. J. Appl. Phys., Part 1 **28**, 1217 (1989).
[8] A. Fissel, J. Cryst. Growth **212**, 438 (2000).
[9] X. Luo, G. Qian, W. Fei, E. G. Wang, and C. Chen, Phys. Rev. B **57**, 9234 (1998).
[10] S. P. Mehandru and A. B. Anderson, Phys. Rev. B **42**, 9040 (1990).
[11] G. Kresse and J. Furthmüller, Phys. Rev. B **54**, 11169 (1996).
[12] G. Kresse and J. Furthmüller, Comput. Mater. Sci. **6**, 15 (1996).
[13] G. Kresse and J. Hafner, J. Phys.: Condens. Matter **6**, 8245 (1994).
[14] G. Kresse and D. Joubert, Phys. Rev. B **59**, 1758 (1999).
[15] J. P. Perdew, J. A. Chevary, S. H. Vosko, K. A. Jackson, M. R. Pederson, D. J. Singh, and C. Fiolhais, Phys. Rev. B **46**, 6671 (1992).
[16] K. Yamamoto, K. Kobayashi, H. Kawanowa, and R. Souda, Phys. Rev. B **60**, 15617 (1999).
[17] U. Grossner, J. Furthmüller, and F. Bechstedt, Phys. Rev. B **64**, 165308 (2001).
[18] P. Vajeeston, P. Ravindran, C. Ravi, and R. Asokamani, Phys. Rev. B **63**, 045115 (2001).
[19] J. C. Boettger, Phys. Rev. B **49**, 16798 (1994).
[20] P.-L. Liu, A. V. G. Chizmeshya, J. Kouvetakis, and I. S. T. Tsong, Phys. Rev. B **72**, 245335 (2005).
[21] J. Furthmüller, P. Käckell, F. Bechstedt, A. Fissel, K. Pfennighaus, B. Schröter, and W. Richter, J. Electron. Mater. **27**, 848 (1998).
[22] J. M. Powers, A. Wander, P. J. Rous, M. A. Van Hove, and G. A. Somorjai, Phys. Rev. B **44**, 11159 (1991).
[23] E. G. Moroni, R. Podloucky, and J. Hafner, Phys. Rev. Lett. **81**, 1969 (1998).
[24] V. Kumar and Y. Kawazoe, Phys. Rev. Lett. **87**, 045503 (2001).
[25] A. Kawamoto, J. Jameson, P. Griffin, C. Kyeongjae, and R. Dutton, IEEE Electron Device Lett. **22**, 14 (2001).
[26] B. Silvi and A. Savin, Nature (London) **371**, 683 (1994).
[27] A. D. Becke and K. E. Edgecombe, J. Chem. Phys. **92**, 5397 (1990).
[28] L. De Santis and R. Resta, Solid State Commun. **111**, 583 (1999).